Progress In Electromagnetics Research, PIER 8, 427–458, 1994

DIFFRACTION BY A PARALLEL-PLATE WAVEGUIDE CAVITY WITH DIELECTRIC/FERRITE LOADING: PART II – THE CASE OF H POLARIZATION

S. Koshikawa and K. Kobayashi

1. Introduction

The scattering from open-ended metallic waveguide cavities is an important subject in radar cross section (RCS) reduction and electromagnetic penetration/coupling studies, since this problem serves as a simple model of duct structures such as jet engine intakes of aircrafts and cracks occurring on surfaces of general complicated bodies. There are a number of analysis methods for treating cavity diffraction problems, but most of them do not rigorously take into account the scattering effect arising from the entire exterior surface of the cavity. In addition, the solutions obtained by these approaches become less accurate when the size of the cavity tends to the low-frequency or the high-frequency limit. In the previous papers [1–3], we have considered a finite parallel-plate waveguide with a planar termination at the open end as an example of simple two-dimensional cavity structures, and solved the plane wave diffraction rigorously by means of the Wiener-

Hopf technique. It has been verified that our final solution is uniformly valid for arbitrary incidence and observation angles as well as for arbitrary cavity dimensions unless the cavity length is too small compared with the wavelength.

In Part I [4] of this two-part paper, we have analyzed, as a generalization to the problem treated in [1–3], the E-polarized plane wave diffraction by a two-dimensional parallel-plate waveguide cavity with dielectric/ferrite loading using the Wiener-Hopf technique. Carrying out numerical computations on the RCS characteristics, it has been shown that, for large cavities, significant RCS reduction can be achieved by lossy material loading inside the cavity. In this second part, the same diffraction problem will be considered for the case of H polarization. Since the method of solution is again based on the Wiener-Hopf technique and is similar to that employed for the E-polarized case, only the main results will be summarized. Our final solution for the field inside the cavity is expressed in terms of the transmitted TM modes, whereas for the field outside the cavity, a far field asymptotic expression is derived using the saddle point method. We shall present representative numerical examples of the monostatic RCS and the bistatic RCS for various physical parameters and discuss the scattering characteristics of the cavity in detail. As in the E-polarized case [4], it is confirmed that the RCS reduction is significant for larger cavities with lossy material loading. We will also show by comparing with the results in Part I that there are some differences on the RCS characteristics depending on the incident polarization. Some comparisons with a high-frequency technique are also included.

The time factor is assumed to be $e^{-i\omega t}$ and suppressed throughout this paper.

2. Transformed Wave Equations

We consider the problem of diffraction of an H-polarized plane wave by a parallel-plate waveguide cavity with dielectric/ferrite loading as shown in Fig. 1, where the H polarization implies that the incident magnetic field is parallel to the y-axis. The cavity plates are assumed to be infinitely thin, perfectly conducting, and uniform in the y-direction, and the material inside the cavity is characterized by the relative permittivity ε_r and the relative permeability μ_r. In view

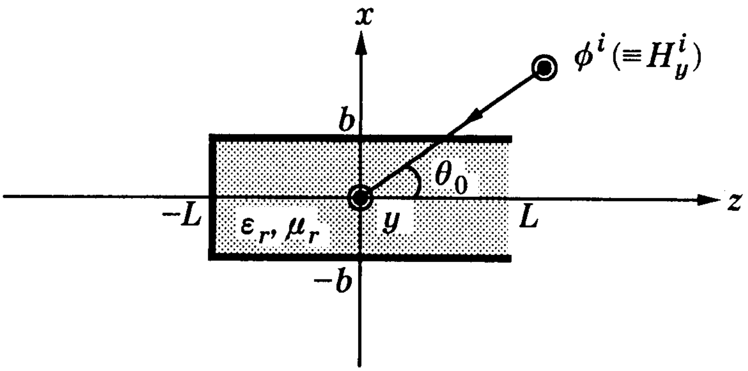

Figure 1. Geometry of the parallel-plate waveguide cavity.

of the geometry and the characteristics of the incident field, this is a two-dimensional problem.

Let the total magnetic field $\phi^t(x,z)[\equiv H_y^t(x,z)]$ be

$$\phi^t(x,z) = \phi^i(x,z) + \phi(x,z), \tag{1}$$

where $\phi^i(x,z)$ is the incident field of H polarization defined by

$$\phi^i(x,z) = e^{-ik(x\sin\theta_0 + z\cos\theta_0)} \tag{2}$$

for $0 < \theta_0 < \pi/2$, and $k[= \omega(\mu_0\varepsilon_0)^{1/2}]$ is the free-space wavenumber. The total field $\phi^t(x,z)$ satisfies the Helmholtz equation:

$$[\partial^2/\partial x^2 + \partial^2/\partial z^2 + \mu(x,z)\varepsilon(x,z)k^2]\phi^t(x,z) = 0, \tag{3}$$

where

$$\mu(x,z) = \begin{cases} 1 & \text{outside the cavity,} \\ \mu_r & \text{inside the cavity,} \end{cases} \tag{4a}$$

$$\varepsilon(x,z) = \begin{cases} 1 & \text{outside the cavity,} \\ \varepsilon_r & \text{inside the cavity.} \end{cases} \tag{4b}$$

Once the solution of (3) has been determined, nonzero components of the total electromagnetic fields are derived from

$$(H_y^t, E_x^t, E_z^t) = \left[\phi^t, \ \frac{1}{i\omega\varepsilon_0\varepsilon(x,z)}\frac{\partial\phi^t}{\partial z}, \ \frac{i}{\omega\varepsilon_0\varepsilon(x,z)}\frac{\partial\phi^t}{\partial x}\right]. \tag{5}$$

For convenience of analysis, we assume that the medium is slightly lossy, i.e., $k = k_1 + ik_2$ with $0 < k_2 \ll k_1$. The solution for real k is obtained by letting $k_2 \to +0$ at the end of analysis. It follows from the radiation condition that $\phi(x,z)$ is $O(e^{-k_2|z|\cos\theta_0})$ as $|z| \to \infty$. Let us define the Fourier transform of the scattered field $\phi(x,z)$ as

$$\Phi(x,\alpha) = (2\pi)^{-1/2} \int_{-\infty}^{\infty} \phi(x,z) e^{i\alpha z} dz, \tag{6}$$

where $\alpha = \mathrm{Re}\,\alpha + i\mathrm{Im}\,\alpha (\equiv \sigma + i\tau)$. Then we see that $\Phi(x,\alpha)$ is regular in the strip $|\tau| < k_2 \cos\theta_0$ of the complex α-plane and is bounded for any α in the strip as $|x| \to \infty$. Introducing the Fourier integrals as

$$\Phi_{\pm}(x,\alpha) = \pm(2\pi)^{-1/2} \int_{\pm L}^{\pm\infty} \phi(x,z) e^{i\alpha(z \mp L)} dz, \tag{7a}$$

$$\Phi_1(x,\alpha) = (2\pi)^{-1/2} \int_{-L}^{L} \phi^t(x,z) e^{i\alpha z} dz, \tag{7b}$$

it is found that $\Phi_+(x,\alpha)$ and $\Phi_-(x,\alpha)$ are regular in the upper half-plane $\tau > -k_2\cos\theta_0$ and the lower half-plane $\tau < k_2 \cos\theta_0$, respectively, whereas $\Phi_1(x,\alpha)$ is an entire function. Using the notation as given by $(7a,b)$, we can express $\Phi(x,\alpha)$ as

$$\Phi(x,\alpha) = \Psi(x,\alpha) + \Phi_1(x,\alpha), \tag{8}$$

where

$$\Psi(x,\alpha) = e^{-i\alpha L}\Psi_-(x,\alpha) + e^{i\alpha L}\Psi_{(+)}(x,\alpha), \tag{9}$$

$$\Psi_-(x,\alpha) = \Phi_-(x,\alpha) + A\frac{e^{-ikx\sin\theta_0}}{\alpha - k\cos\theta_0}, \tag{10a}$$

$$\Psi_{(+)}(x,\alpha) = \Phi_+(x,\alpha) - B\frac{e^{-ikx\sin\theta_0}}{\alpha - k\cos\theta_0}, \tag{10b}$$

$$A = \frac{e^{ikL\cos\theta_0}}{(2\pi)^{1/2}\,i}, \qquad B = \frac{e^{-ikL\cos\theta_0}}{(2\pi)^{1/2}\,i}. \tag{11}$$

The parentheses in the subscript of $\Psi_{(+)}(x,\alpha)$ defined by (10b) imply that $\Psi_{(+)}(x,\alpha)$ is regular in $\tau > -k_2\cos\theta_0$ except at a simple pole $\alpha = k\cos\theta_0$.

Let us now derive transformed wave equations by following a procedure similar to that developed in Part I. For the region $|x| > b$, we can show by taking the Fourier transform of the Helmholtz equation for the scattered field that

$$(d^2/dx^2 - \gamma^2)\Phi(x, \alpha) = 0 \tag{12}$$

holds for any α in the strip $|\tau| < k_2 \cos\theta_0$, where $\gamma = (\alpha^2 - k^2)^{1/2}$. We choose a proper branch for the double-valued function γ such that γ reduces to $-ik$ when $\alpha = 0$. Equation (12) is the transformed wave equation for $|x| > b$.

For the region $|x| < b$, we first multiply both sides of the Helmholtz equation for the scattered field by $(2\pi)^{-1/2}e^{i\alpha z}$ and integrate with respect to z over the ranges $-\infty < z < -L$ and $L < z < \infty$. Then by taking into account the boundary condition at $z = \pm L$, we derive that

$$(d^2/dx^2 - \gamma^2)\Psi_-(x, \alpha) = i\alpha g_1^-(x) \tag{13}$$

for $\tau < k_2 \cos\theta_0$, and that

$$(d^2/dx^2 - \gamma^2)\Psi_{(+)}(x, \alpha) = \varepsilon_r^{-1} f(x) - i\alpha g_2(x) \tag{14}$$

for $\tau > -k_2 \cos\theta_0$, with $\alpha \neq k\cos\theta_0$, where

$$f(x) = (2\pi)^{-1/2}\frac{\partial\phi^t(x, L-0)}{\partial z}, \tag{15a}$$

$$g_1^{\pm}(x) = (2\pi)^{-1/2}\phi^t(x, -L \pm 0), \tag{15b}$$

$$g_2(x) = (2\pi)^{-1/2}\phi^t(x, L). \tag{15c}$$

We also multiply both sides of the Helmholtz equation for the total field by $(2\pi)^{-1/2}e^{i\alpha z}$ and integrate with respect to z over the range $-L < z < L$. This gives, after making use of the boundary condition at $z = \pm L$,

$$(d^2/dx^2 - \Gamma^2)\Phi_1(x, \alpha) = e^{-i\alpha L} i\alpha g_1^+(x) - e^{i\alpha L}[f(x) - i\alpha g_2(x)] \tag{16}$$

for all α, where $\Gamma = (\alpha^2 - k_r^2)^{1/2}$ with $k_r = (\mu_r \varepsilon_r)^{1/2}k$. The proper branch for Γ is chosen such that Γ reduces to $-ik_r$ when $\alpha = 0$.

Equations (13), (14), and (16) are the transformed wave equations for $|x| < b$, where the unknown inhomogeneous terms have appeared due to the medium discontinuities across $z = \pm L$.

3. Simultaneous Wiener-Hopf Equations

In this section, we shall formulate the problem in terms of the simultaneous Wiener-Hopf equations by imposing boundary conditions appropriately. To this end, it is convenient to solve the transformed wave equations (12)–(14) and (16) to derive a scattered field representation in the Fourier transform domain. First let us consider the region $|x| > b$. Since $\Phi(x, \alpha)$ is bounded as $|x| \to \infty$, the solution of (12) is expressed as

$$\Phi(x,\alpha) = \begin{cases} -\Psi'(b,\alpha)\gamma^{-1}e^{-\gamma(x-b)} & \text{for} \quad x > b, \\ \Psi'(-b,\alpha)\gamma^{-1}e^{\gamma(x+b)} & \text{for} \quad x < -b \end{cases} \tag{17}$$

by taking into account the boundary condition for tangential electric fields across $x = \pm b$, where the prime denotes differentiation with respect to x. Equation (17) gives a scattered field representation for $|x| > b$.

Next we consider the region $|x| < b$. In view of the edge condition, it is seen that the unknown inhomogeneous terms $f(x), g_1^{\pm}(x)$, and $g_2(x)$ defined by ($15a, b, c$) are absolutely integrable over the range $|x| \le b$. We now expand these inhomogeneous terms into the convergent Fourier cosine series as in

$$f(x) = \frac{1}{b}\sum_{n=0}^{\infty} \delta_n f_n \cos\frac{n\pi}{2b}(x+b), \tag{18a}$$

$$g_1^{\pm}(x) = \frac{1}{b}\sum_{n=0}^{\infty} \delta_n g_{1n}^{\pm} \cos\frac{n\pi}{2b}(x+b), \tag{18b}$$

$$g_2(x) = \frac{1}{b}\sum_{n=0}^{\infty} \delta_n g_{2n} \cos\frac{n\pi}{2b}(x+b) \tag{18c}$$

for $|x| < b$, where

$$\delta_0 = 1/2; \qquad \delta_n = 1 \qquad \text{for } n \ge 1. \tag{19}$$

Taking into account $(18a, b, c)$ and following a procedure similar to that developed in Part I, we arrive at the solutions of (13), (14), and (16) with the result that

$$\Psi_-(x,\alpha) = \Psi'_-(b,\alpha)\frac{\cosh\gamma(x+b)}{\gamma\sinh 2\gamma b} - \Psi'_-(-b,\alpha)\frac{\cosh\gamma(x-b)}{\gamma\sinh 2\gamma b}$$
$$-\frac{1}{b}\sum_{n=0}^{\infty}\delta_n\frac{i\alpha g^-_{1n}}{\alpha^2+\gamma_n^2}\cos\frac{n\pi}{2b}(x+b), \tag{20}$$

$$\Psi_{(+)}(x,\alpha) = \Psi'_{(+)}(b,\alpha)\frac{\cosh\gamma(x+b)}{\gamma\sinh 2\gamma b} - \Psi'_{(+)}(-b,\alpha)\frac{\cosh\gamma(x-b)}{\gamma\sinh 2\gamma b}$$
$$-\frac{1}{b}\sum_{n=0}^{\infty}\delta_n\frac{c_n^+(\alpha)}{\alpha^2+\gamma_n^2}\cos\frac{n\pi}{2b}(x+b), \tag{21}$$

$$\Phi_1(x,\alpha) = \frac{1}{b}\sum_{n=0}^{\infty}\delta_n\frac{e^{-i\alpha L}i\alpha g^+_{1n} + e^{i\alpha L}c_n^-(\alpha)}{\alpha^2+\Gamma_n^2}\cos\frac{n\pi}{2b}(x+b), \tag{22}$$

where

$$\gamma_0 = -ik; \qquad \gamma_n = [(n\pi/2b)^2 - k^2]^{1/2} \qquad \text{for } n \geq 1, \tag{23a}$$
$$\Gamma_0 = -ik_r; \qquad \Gamma_n = [(n\pi/2b)^2 - k_r^2]^{1/2} \qquad \text{for } n \geq 1, \tag{23b}$$

$$c_n^+(\alpha) = \varepsilon_r^{-1}f_n - i\alpha g_{2n}, \qquad c_n^-(\alpha) = f_n - i\alpha g_{2n}. \tag{24}$$

According to the definition, $\Psi_-(x,\alpha)$ is regular in $\tau < k_2\cos\theta_0$ and $\Psi_{(+)}(x,\alpha)$ is regular in $\tau > -k_2\cos\theta_0$ except for a simple pole at $\alpha = k\cos\theta_0$, whereas $\Phi_1(x,\alpha)$ is an entire function. In particular, it follows that (20), (21), and (22) tend to finite limits as $\alpha \to -i\gamma_m, i\gamma_m$, and $\pm i\Gamma_m$ with $m = 0, 1, 2, \cdots$, respectively. Therefore, we deduce, after some manipulations, that the Fourier coefficients $f_n, g^{\pm}_{1n}$ and g_{2n} in $(18a, b, c)$ are expressed as

$$f_n = \begin{cases} -P_n U_{(+)}(i\gamma_n) & \text{for odd } n, \\ P_n V_{(+)}(i\gamma_n) & \text{for even } n, \end{cases} \tag{25}$$

$$g_{1n}^{-} = \begin{cases} -U_{-}(-i\gamma_n)/\gamma_n & \text{for odd } n, \\ V_{-}(-i\gamma_n)/\gamma_n & \text{for even } n, \end{cases} \tag{26a}$$

$$g_{1n}^{+} = \begin{cases} -Q_n U_{(+)}(i\gamma_n) & \text{for odd } n, \\ Q_n V_{(+)}(i\gamma_n) & \text{for even } n, \end{cases} \tag{26b}$$

$$g_{2n} = \begin{cases} -R_n U_{(+)}(i\gamma_n) & \text{for odd } n, \\ R_n V_{(+)}(i\gamma_n) & \text{for even } n, \end{cases} \tag{27}$$

where

$$U_{-}(\alpha) = \Psi'_{-}(b,\alpha) + \Psi'_{-}(-b,\alpha), \tag{28a}$$

$$U_{(+)}(\alpha) = \Psi'_{(+)}(b,\alpha) + \Psi'_{(+)}(-b,\alpha), \tag{28b}$$

$$V_{-}(\alpha) = \Psi'_{-}(b,\alpha) - \Psi'_{-}(-b,\alpha), \tag{29a}$$

$$V_{(+)}(\alpha) = \Psi'_{(+)}(b,\alpha) - \Psi'_{(+)}(-b,\alpha), \tag{29b}$$

$$P_n = \frac{\varepsilon_r \Gamma_n}{\varepsilon_r \gamma_n + \Gamma_n} \frac{1 - e^{-4\Gamma_n L}}{1 + \rho_n e^{-4\Gamma_n L}}, \tag{30a}$$

$$Q_n = \frac{2\varepsilon_r}{\varepsilon_r \gamma_n + \Gamma_n} \frac{e^{-2\Gamma_n L}}{1 + \rho_n e^{-4\Gamma_n L}}, \tag{30b}$$

$$R_n = \frac{\varepsilon_r}{\varepsilon_r \gamma_n + \Gamma_n} \frac{1 + e^{-4\Gamma_n L}}{1 + \rho_n e^{-4\Gamma_n L}}, \tag{30c}$$

$$\rho_n = (\varepsilon_r \gamma_n - \Gamma_n)/(\varepsilon_r \gamma_n + \Gamma_n). \tag{31}$$

Substituting (20) and (21) into (9) and using (8) and (22), a scattered field representation for $|x| < b$ will be derived.

Summarizing the above results, an explicit expression for $\Phi(x,\alpha)$ is given by

$$
\Phi(x,\alpha) = \begin{cases}
-\Psi'(b,\alpha)\gamma^{-1}e^{-\gamma(x-b)} & \text{for} \quad x > b, \\
\Psi'(-b,\alpha)\gamma^{-1}e^{\gamma(x+b)} & \text{for} \quad x < -b, \\
\Psi'(b,\alpha)\dfrac{\cosh\gamma(x+b)}{\gamma\sinh 2\gamma b} - \Psi'(-b,\alpha)\dfrac{\cosh\gamma(x-b)}{\gamma\sinh 2\gamma b} & \\
\quad -\dfrac{1}{b}\displaystyle\sum_{n=0}^{\infty}\delta_n \dfrac{e^{-i\alpha L} i\alpha g_{1n}^{-} + e^{i\alpha L} c_n^{+}(\alpha)}{\alpha^2+\gamma_n^2}\cos\dfrac{n\pi}{2b}(x+b) & \\
\quad +\dfrac{1}{b}\displaystyle\sum_{n=0}^{\infty}\delta_n \dfrac{e^{-i\alpha L} i\alpha g_{1n}^{+} + e^{i\alpha L} c_n^{-}(\alpha)}{\alpha^2+\Gamma_n^2}\cos\dfrac{n\pi}{2b}(x+b) & \text{for} \quad |x| < b.
\end{cases}
\tag{32}
$$

Setting $x = b \pm 0$ and $-b \pm 0$ in (32) and taking into account the boundary condition for tangential magnetic fields across $x = \pm b$ with $|z| > L$, we derive that

$$
\begin{aligned}
J_1^d(\alpha) = &-\frac{e^{-i\alpha L}U_{-}(\alpha) + e^{i\alpha L}U_{(+)}(\alpha)}{M(\alpha)} \\
&-\frac{2}{b}\sum_{n=1,\text{odd}}^{\infty}\frac{e^{-i\alpha L} i\alpha g_{1n}^{-} + e^{i\alpha L} c_n^{+}(\alpha)}{\alpha^2+\gamma_n^2} \\
&+\frac{2}{b}\sum_{n=1,\text{odd}}^{\infty}\frac{e^{-i\alpha L} i\alpha g_{1n}^{+} + e^{i\alpha L} c_n^{-}(\alpha)}{\alpha^2+\Gamma_n^2},
\end{aligned}
\tag{33}
$$

$$
\begin{aligned}
J_1^s(\alpha) = &-\frac{e^{-i\alpha L}V_{-}(\alpha) + e^{i\alpha L}V_{(+)}(\alpha)}{N(\alpha)} \\
&+\frac{2}{b}\sum_{n=0,\text{even}}^{\infty}\delta_n\frac{e^{-i\alpha L} i\alpha g_{1n}^{-} + e^{i\alpha L} c_n^{+}(\alpha)}{\alpha^2+\gamma_n^2} \\
&-\frac{2}{b}\sum_{n=0,\text{even}}^{\infty}\delta_n\frac{e^{-i\alpha L} i\alpha g_{1n}^{+} + e^{i\alpha L} c_n^{-}(\alpha)}{\alpha^2+\Gamma_n^2}
\end{aligned}
\tag{34}
$$

for $|\tau| < k_2\cos\theta_0$, where

$$J_1^d(\alpha) = J_1(b,\alpha) - J_1(-b,\alpha), \tag{35a}$$

$$J_1^s(\alpha) = J_1(b,\alpha) + J_1(-b,\alpha), \tag{35b}$$

$$J_1(\pm b, \alpha) = \Phi_1(\pm b \pm 0, \alpha) - \Phi_1(\pm b \mp 0, \alpha), \tag{36}$$

$$M(\alpha) = \gamma e^{-\gamma b} \cosh \gamma b, \qquad N(\alpha) = \gamma e^{-\gamma b} \sinh \gamma b. \tag{37}$$

Equations (33) and (34) are the simultaneous Wiener-Hopf equations satisfied by the unknown spectral functions, where an infinite number of unknowns are also involved.

4. Exact and Approximate Solutions

According to the standard literature [5–7], the kernel functions $M(\alpha)$ and $N(\alpha)$ defined by (37) are factorized as follows:

$$M(\alpha) = M_+(\alpha)M_-(\alpha) = M_+(\alpha)M_+(-\alpha), \tag{38a}$$

$$N(\alpha) = N_+(\alpha)N_-(\alpha) = N_+(\alpha)N_+(-\alpha), \tag{38b}$$

where

$$\begin{aligned} M_+(\alpha) =& (\cos kb)^{1/2} e^{i3\pi/4} (k+\alpha)^{1/2} \exp\left(\frac{i\gamma b}{\pi} \ln \frac{\alpha - \gamma}{k}\right) \\ & \cdot \exp\left[\frac{i\alpha b}{\pi}\left(1 - C + \ln \frac{\pi}{2kb} + i\frac{\pi}{2}\right)\right] \\ & \cdot \prod_{n=1,\text{odd}}^{\infty} \left(1 + \frac{\alpha}{i\gamma_n}\right) e^{2i\alpha b/n\pi}, \end{aligned} \tag{39a}$$

$$\begin{aligned} N_+(\alpha) =& (k \sin kb)^{1/2} e^{i\pi/2} \exp\left(\frac{i\gamma b}{\pi} \ln \frac{\alpha - \gamma}{k}\right)\left(1 + \frac{\alpha}{i\gamma_0}\right) \\ & \cdot \exp\left[\frac{i\alpha b}{\pi}\left(1 - C + \ln \frac{2\pi}{kb} + i\frac{\pi}{2}\right)\right] \\ & \cdot \prod_{n=2,\text{even}}^{\infty} \left(1 + \frac{\alpha}{i\gamma_n}\right) e^{2i\alpha b/n\pi}. \end{aligned} \tag{39b}$$

In $(39a, b), C (= 0.57721566 \cdots)$ is Euler's constant. It is seen from $(38a, b)$ and $(39a, b)$ that the split functions $M_\pm(\alpha)$ and $N_\pm(\alpha)$ are regular and nonzero in $\tau \gtrless \mp k_2$, and show the asymptotic behavior

$$M_\pm(\alpha) \sim -(\mp i\alpha/2)^{1/2}, \qquad N_\pm(\alpha) \sim -(\mp i\alpha/2)^{1/2} \tag{40}$$

as $\alpha \to \infty$ with $\tau \gtrless \mp k_2$.

We multiply both sides of (33) and (34) by $e^{\pm i\alpha L}M_{\pm}(\alpha)$ and $e^{\pm i\alpha L}N_{\pm}(\alpha)$, respectively, and apply the decomposition procedure. Omitting the whole details, we arrive at the following result:

$$
\begin{aligned}
U_{-}(\alpha) = {} & b^{1/2}M_{-}(\alpha)\left[\frac{A_u}{b(\alpha - k\cos\theta_0)} + \frac{J_u^{(1)}(\alpha)}{b^{1/2}}\right. \\
& \left. - \sum_{n=2}^{\infty} \frac{a_n p_n u_n^{-}}{b(\alpha - i\gamma_{2n-3})}\right],
\end{aligned} \tag{41a}
$$

$$
\begin{aligned}
U_{(+)}(\alpha) = {} & b^{1/2}M_{+}(\alpha)\left[-\frac{B_u}{b(\alpha - k\cos\theta_0)} + \frac{J_u^{(2)}(\alpha)}{b^{1/2}}\right. \\
& \left. - \sum_{n=2}^{\infty} \frac{\kappa_{2n-3} a_n p_n u_n^{+}}{b(\alpha + i\gamma_{2n-3})}\right],
\end{aligned} \tag{41b}
$$

$$
\begin{aligned}
V_{-}(\alpha) = {} & b^{1/2}N_{-}(\alpha)\left[-\frac{A_v}{b(\alpha - k\cos\theta_0)} + \frac{J_v^{(1)}(\alpha)}{b^{1/2}}\right. \\
& \left. - \sum_{n=1}^{\infty} \frac{\delta_{2n-2} b_n q_n v_n^{-}}{b(\alpha - i\gamma_{2n-2})}\right],
\end{aligned} \tag{42a}
$$

$$
\begin{aligned}
V_{(+)}(\alpha) = {} & b^{1/2}N_{+}(\alpha)\left[\frac{B_v}{b(\alpha - k\cos\theta_0)} + \frac{J_v^{(2)}(\alpha)}{b^{1/2}}\right. \\
& \left. - \sum_{n=1}^{\infty} \frac{\delta_{2n-2}\kappa_{2n-2} b_n q_n v_n^{+}}{b(\alpha + i\gamma_{2n-2})}\right],
\end{aligned} \tag{42b}
$$

where

$$
\kappa_n = -\frac{\rho_n + e^{-4\Gamma_n L}}{1 + \rho_n e^{-4\Gamma_n L}}, \tag{43}
$$

$$
a_1 = (bi\gamma_0)^{-1}; \qquad a_n = (bi\gamma_{2n-3})^{-1} \quad \text{for } n \geq 2, \tag{44a}
$$

$$
b_1 = (bi\gamma_0)^{-1}; \qquad b_n = (bi\gamma_{2n-2})^{-1} \quad \text{for } n \geq 2, \tag{44b}
$$

$$
p_1 = b^{1/2}M_{+}(i\gamma_0); \qquad p_n = b^{1/2}M_{+}(i\gamma_{2n-3}) \quad \text{for } n \geq 2, \tag{45a}
$$

$$
q_1 = b^{1/2}N_{+}(i\gamma_0); \qquad q_n = b^{1/2}N_{+}(i\gamma_{2n-2}) \quad \text{for } n \geq 2, \tag{45b}
$$

$$u_1^- = U_-(-i\gamma_0); \qquad u_n^- = U_-(-i\gamma_{2n-3}) \quad \text{for } n \geq 2, \tag{46a}$$

$$u_1^+ = U_{(+)}(i\gamma_0); \qquad u_n^+ = U_{(+)}(i\gamma_{2n-3}) \quad \text{for } n \geq 2, \tag{46b}$$

$$v_1^- = V_-(-i\gamma_0); \qquad v_n^- = V_-(-i\gamma_{2n-2}) \quad \text{for } n \geq 2, \tag{47a}$$

$$v_1^+ = V_{(+)}(i\gamma_0); \qquad v_n^+ = V_{(+)}(i\gamma_{2n-2}) \quad \text{for } n \geq 2, \tag{47b}$$

$$A_u = \frac{2A' \cos(kb \sin\theta_0)}{b^{1/2} M_-(k\cos\theta_0)}, \qquad B_u = \frac{2B' \cos(kb\sin\theta_0)}{b^{1/2} M_+(k\cos\theta_0)}, \tag{48}$$

$$A_v = \frac{2iA' \sin(kb\sin\theta_0)}{b^{1/2} N_-(k\cos\theta_0)}, \qquad B_v = \frac{2iB' \sin(kb\sin\theta_0)}{b^{1/2} N_+(k\cos\theta_0)}, \tag{49}$$

$$J_u^{(1)}(\alpha) = \frac{1}{\pi i}\int_k^{k+i\infty} e^{2i\beta L} \frac{M_+(\beta) U_{(+)}(\beta)}{(\beta^2 - k^2)^{1/2}(\beta - \alpha)} d\beta, \tag{50a}$$

$$J_u^{(2)}(\alpha) = \frac{1}{\pi i}\int_k^{k+i\infty} e^{2i\beta L} \frac{M_+(\beta) U_-(-\beta)}{(\beta^2 - k^2)^{1/2}(\beta + \alpha)} d\beta, \tag{50b}$$

$$J_v^{(1)}(\alpha) = \frac{1}{\pi i}\int_k^{k+i\infty} e^{2i\beta L} \frac{N_+(\beta) V_{(+)}(\beta)}{(\beta^2 - k^2)^{1/2}(\beta - \alpha)} d\beta, \tag{51a}$$

$$J_v^{(2)}(\alpha) = \frac{1}{\pi i}\int_k^{k+i\infty} e^{2i\beta L} \frac{N_+(\beta) V_-(-\beta)}{(\beta^2 - k^2)^{1/2}(\beta + \alpha)} d\beta, \tag{51b}$$

$$A' = -\frac{kb\sin\theta_0 e^{ikL\cos\theta_0}}{(2\pi)^{1/2}}, \qquad B' = -\frac{kb\sin\theta_0 e^{-ikL\cos\theta_0}}{(2\pi)^{1/2}}. \tag{52}$$

In $(50a, b)$ and $(51a, b)$, a branch cut for $(\beta^2 - k^2)^{1/2}$ has been chosen as a straight line parallel to the imaginary axis, extending from $\beta = k$ to infinity in the upper half-plane. The contour for these infinite integrals is a straight path on the right-hand side of the branch cut. Equations $(41a, b)$ and $(42a, b)$ are the formal solution to the Wiener-Hopf equations (33) and (34), where the infinite series with the unknowns $u_n^\pm$ for $n = 2, 3, 4, \cdots$ and $v_n^\pm$ for $n = 1, 2, 3, \cdots$, as well as the branch-cut integrals $J_u^{(1)}(\alpha), J_u^{(2)}(\alpha), J_v^{(1)}(\alpha)$, and $J_v^{(2)}(\alpha)$ with unknown integrands, are involved.

Employing rigorous asymptotics similar to those for the E-polarized case treated in Part I, approximate expressions of (41a, b) and (42a, b) are obtained as follows:

$$\begin{aligned} U_-(\alpha) \approx b^{1/2} M_-(\alpha) \Bigg(& \frac{A_u}{b(\alpha - k\cos\theta_0)} \\ & + a_1 p_1 \left\{ \left[u_1^+ + \frac{2B' \cos(kb\sin\theta_0)}{kb(1-\cos\theta_0)} \right] \xi(-\alpha) \right. \\ & \left. + \frac{2B'L}{b} \cos(kb\sin\theta_0) \chi(-\alpha, -k\cos\theta_0) \right\} \\ & - \sum_{n=2}^{N-1} \frac{a_n p_n u_n^-}{b(\alpha - i\gamma_{2n-3})} - K_u^{(1)} S_{uN}^{(1)}(\alpha) \Bigg), \end{aligned} \tag{53a}$$

$$\begin{aligned} U_{(+)}(\alpha) \approx b^{1/2} M_+(\alpha) \Bigg(& -\frac{B_u}{b(\alpha - k\cos\theta_0)} \\ & + a_1 p_1 \left\{ \left[u_1^- + \frac{2A' \cos(kb\sin\theta_0)}{kb(1+\cos\theta_0)} \right] \xi(\alpha) \right. \\ & \left. + \frac{2A'L}{b} \cos(kb\sin\theta_0) \chi(\alpha, k\cos\theta_0) \right\} \\ & - \sum_{n=2}^{N-1} \frac{\kappa_{2n-3} a_n p_n u_n^+}{b(\alpha + i\gamma_{2n-3})} - K_u^{(2)} S_{uN}^{(2)}(\alpha) \Bigg), \end{aligned} \tag{53b}$$

$$\begin{aligned} V_-(\alpha) \approx b^{1/2} N_-(\alpha) \Bigg(& -\frac{A_v}{b(\alpha - k\cos\theta_0)} \\ & + b_1 q_1 \left\{ \left[v_1^+ - \frac{2iB' \sin(kb\sin\theta_0)}{kb(1-\cos\theta_0)} \right] \xi(-\alpha) \right. \\ & \left. - \frac{2iB'L}{b} \sin(kb\sin\theta_0) \chi(-\alpha, -k\cos\theta_0) \right\} \\ & - \sum_{n=1}^{N-1} \frac{\delta_{2n-2} b_n q_n v_n^-}{b(\alpha - i\gamma_{2n-2})} - K_u^{(1)} S_{vN}^{(1)}(\alpha) \Bigg), \end{aligned} \tag{54a}$$

$$\begin{aligned} V_{(+)}(\alpha) \approx b^{1/2} N_{+}(\alpha) \Bigg(& \frac{B_v}{b(\alpha - k\cos\theta_0)} \\ & + b_1 q_1 \Bigg\{ \left[v_1^- - \frac{2iA' \sin(kb\sin\theta_0)}{kb(1+\cos\theta_0)} \right] \xi(\alpha) \\ & - \frac{2iA'L}{b} \sin(kb\sin\theta_0) \chi(\alpha, k\cos\theta_0) \Bigg\} \\ & - \sum_{n=1}^{N-1} \frac{\delta_{2n-2}\kappa_{2n-2} b_n q_n v_n^+}{b(\alpha + i\gamma_{2n-2})} - K_v^{(2)} S_{vN}^{(2)}(\alpha) \Bigg), \end{aligned} \tag{54b}$$

where

$$\xi(\alpha) = \frac{(kL)^{1/2} e^{i(2kL - 3\pi/4)}}{\pi} \Gamma_1[1/2, -2i(\alpha + k)L], \tag{55}$$

$$\chi(\alpha, \beta) = \frac{\xi(\alpha) - \xi(\beta)}{(\alpha - \beta)L}, \tag{56}$$

$$S_{uN}^{(1)}(\alpha) = \sum_{n=N}^{\infty} \frac{(b\gamma_{2n-3})^{-7/6}}{b(\alpha - i\gamma_{2n-3})}, \tag{57a}$$

$$S_{uN}^{(2)}(\alpha) = \sum_{n=N}^{\infty} \frac{\kappa_{2n-3}(b\gamma_{2n-3})^{-1/2-\nu}}{b(\alpha + i\gamma_{2n-3})}, \tag{57b}$$

$$S_{vN}^{(1)}(\alpha) = \sum_{n=N}^{\infty} \frac{(b\gamma_{2n-2})^{-7/6}}{b(\alpha - i\gamma_{2n-2})}, \tag{58a}$$

$$S_{vN}^{(2)}(\alpha) = \sum_{n=N}^{\infty} \frac{\kappa_{2n-2}(b\gamma_{2n-2})^{-1/2-\nu}}{b(\alpha + i\gamma_{2n-2})}. \tag{58b}$$

In (55), $\Gamma_1(\cdot, \cdot)$ is the generalized gamma function [2, 8] defined by

$$\Gamma_m(u, v) = \int_0^{\infty} \frac{t^{u-1} e^{-t}}{(t + v)^m} \, dt \tag{59}$$

for $\operatorname{Re} u > 0$, $|v| > 0$, $|\arg v| < \pi$, and positive integer m. In the derivation of (53a, b) and (54a, b), it has been taken into account that, in view of Meixner's edge condition [6, 9], the unknowns $u_n^{\pm}$ and $v_n^{\pm}$ defined by $(46a, b)$ and $(47a, b)$ show the asymptotic behavior

$$u_n^- \sim -2^{1/2} i K_u^{(1)} (b\gamma_{2n-3})^{-2/3}, \quad u_n^+ \sim -2^{1/2} i K_u^{(2)} (b\gamma_{2n-3})^{-\nu}, \qquad (60a)$$

$$v_n^- \sim -2^{1/2} i K_v^{(1)} (b\gamma_{2n-2})^{-2/3}, \quad v_n^+ \sim -2^{1/2} i K_v^{(2)} (b\gamma_{2n-2})^{-\nu} \qquad (60b)$$

as $n \to \infty$, where

$$\nu = \eta(\nu_\mu + 1,\ \nu_\varepsilon), \qquad \mathrm{Re}\,\nu > 0 \qquad (61)$$

with

$$\nu_\mu = \frac{1}{\pi} \cos^{-1} \frac{\mu_r - 1}{2(\mu_r + 1)}, \qquad \nu_\varepsilon = \frac{1}{\pi} \cos^{-1} \frac{1 - \varepsilon_r}{2(1 + \varepsilon_r)}, \qquad (62)$$

$$\eta(a, b) = \begin{cases} a & \text{for } \mathrm{Re}\,a \le \mathrm{Re}\,b, \\ b & \text{for } \mathrm{Re}\,a \ge \mathrm{Re}\,b. \end{cases} \qquad (63)$$

In (62), the inverse cosine functions should be interpreted as the principal value. Equations $(53a, b)$ and $(54a, b)$ give the approximate solution to the Wiener-Hopf equations (33) and (34), and they hold uniformly in θ_0 for large positive integer N and large $|k|L$. The unknowns $u_n^{\pm}$ and $v_n^{\pm}$ for $n = 1, 2, 3, \cdots, N-1$ as well as $K_u^{(1)}, K_u^{(2)}, K_v^{(1)}$, and $K_v^{(2)}$ are involved in $(53a, b)$ and $(54a, b)$, which can be determined with high accuracy by solving appropriate matrix equations numerically [4]. It should be noted that the above approximate solution is valid over wide frequency range as long as the cavity depth $2L$ is not too small compared with the wavelength.

5. Scattered Field

The scattered field can be derived by taking the inverse Fourier transform of (32) according to the formula:

$$\phi(x, z) = (2\pi)^{-1/2} \int_{-\infty + ic}^{\infty + ic} \Phi(x, \alpha) e^{-i\alpha z}\, d\alpha, \qquad (64)$$

where $|c| < k_2 \cos\theta_0$. First let us consider the field inside the cavity. Substituting the field representation for $|x| < b$ in (32) to (64) and evaluating the resultant integral with the aid of (25), (26a, b), and (27), we derive, after some manipulations, that

$$\phi(x,z) = -\, e^{-ik(x\sin\theta_0 + z\cos\theta_0)} + \sum_{n=0}^{\infty} T_n \cos\frac{n\pi}{2b}(x+b)\cosh\Gamma_n(z+L), \tag{65}$$

where

$$T_n = \begin{cases} -(2\pi)^{1/2}\,\frac{Q_n}{b}\,U_{(+)}(i\gamma_n) & \text{for odd } n, \\ (2\pi)^{1/2}\,\delta_n\,\frac{Q_n}{b}\,V_{(+)}(i\gamma_n) & \text{for even } n. \end{cases} \tag{66}$$

In (65), the first term exactly cancels the incident field defined by (2), and the second term represents the transmitted TM modes coupling into the cavity. In view of (46b) and (47b), we see that T_0, T_{2n-3}, and T_{2n-2} with $n = 2, 3, 4, \cdots$ are expressed using v_1^+, u_n^+, and v_n^+, respectively.

Next we shall consider the field outside the cavity and derive the scattered far field. The region outside the cavity includes $|z| > L$ with $|x| < b$, but this region is of less interest in the far field from a practical point of view. Therefore, the derivation of the scattered far field only for $|x| > b$ will be discussed in the following. Using the field representation for $|x| > b$ in (32) and evaluating its inverse Fourier transform asymptotically with the aid of the saddle point method, the scattered far field is found to be

$$\phi(\rho,\theta) \sim \pm\Psi'(\pm b, -k\cos\theta)e^{\mp ikb\sin\theta}\,\frac{e^{i(k\rho-3\pi/4)}}{(k\rho)^{1/2}} \tag{67}$$

for $x \gtrless \pm b$ as $k\rho \to \infty$, where (ρ,θ) is the polar coordinate defined by $x = \rho\sin\theta, z = \rho\cos\theta$ for $0 < |\theta| < \pi$. In (67), $\Psi'(\pm b, \alpha)$ can be expressed as

$$\Psi'(\pm b,\alpha) = e^{-i\alpha L}\frac{U_-(\alpha) \pm V_-(\alpha)}{2} + e^{i\alpha L}\frac{U_{(+)}(\alpha) \pm V_{(+)}(\alpha)}{2} \tag{68}$$

by making use of (9), (28a, b), and (29a, b). Although the analysis has been carried out by assuming $0 < \theta_0 < \pi/2$, the results remain valid for arbitrary θ_0.

6. Numerical Results and Discussion

In this section, we shall present numerical examples of the monostatic RCS and the bistatic RCS to discuss the far field scattering characteristics of the cavity in detail. Numerical results presented below are all based on the scattered far field expression given by (67) together with (68). We have used the approximate expressions as derived in (53a, b) and (54a, b) for computation of $U_-(\alpha), U_{(+)}(\alpha)$, $V_-(\alpha)$, and $V_{(+)}(\alpha)$ involved in (68). Since the problem under consideration is of the two-dimensional scattering, the RCS per unit length is defined by

$$\sigma = \lim_{\rho \to \infty} \left(2\pi\rho \frac{|\phi|^2}{|\phi^i|^2} \right). \tag{69}$$

For real k, (69) is simplified using (67) as

$$\sigma = \lambda |\Psi'(\pm b, -k\cos\theta)|^2 \tag{70}$$

for $\theta \gtrless 0$ with λ being the free-space wavelength. Figures 2–4 and 5–7 show numerical results of the monostatic RCS versus the incidence angle θ_0 and the bistatic RCS versus the observation angle θ, respectively, where the values of σ/λ are plotted in decibels [dB] by computing $10\log_{10}\sigma/\lambda$. As in the E-polarized case treated in Part I [4], the incidence angle θ_0 has been fixed as 60° in the bistatic RCS computations, and the ratio L/b is taken to be 1.0, 2.0, and 3.0. For each L/b, numerical computations have been carried out by choosing three different values of the cavity opening as $2b = \lambda, 5\lambda$, and 10λ. The ferrite with $\varepsilon_r = 2.5 + i1.25$ and $\mu_r = 1.6 + i0.8$ [10] has been taken as an example of lossy materials, and the previous results for empty cavities [3] have been added by dashed lines to investigate the effect of material loading inside the cavity.

From Figs. 2–4, we observe that, as in the E-polarized case, there are noticeable peaks at $\theta_0 = 90°$ and $180°$ in all examples which are due to the specular reflection from the sideplate surface at $x = b + 0$ and from the endplate surface at $z = -L - 0$, respectively. The other common feature between the E and the H polarization is that, the RCS characteristics for both empty and loaded cavities show nearly identical features over the range $90° \le \theta_0 \le 180°$, whereas there is obviously a difference in the scattering characteristics over the range $0° \le \theta_0 \le 90°$ depending on the material inside the cavity. Hence, it is confirmed that when the cavity aperture is visible (invisible) from the source point, main contributions to the backscattered far field arise from the interior (exterior) features of the cavity structure. In particular, for cavities of $2b = 5\lambda$ and 10λ with no material loading, the monostatic RCS exhibits fairly large values within the range $0° \leq \theta_0 \leq 70°$ due to the interior irradiation, whereas the irradiation is reduced for the case of material loading. It is also noted that this RCS reduction is significant for larger cavities as in the E polarization. Let us now make comparisons of the monostatic RCS between the E and the H polarization in some more detail, and investigate the difference on the backscattering characteristics due to the incident polarization. First we consider the region $90° \leq \theta_0 \leq 180°$ where the cavity aperture is invisible from the source point. In this region, main contributions to the far field backscattering will be edge-diffracted fields except in the neighborhood of $\theta_0 = 90°$ and $180°$. Comparing the RCS curves over $90° \leq \theta_0 \leq 180°$ in Figs. 2–4 for the H polarization with those in Figs. I.4–I.6 (prefix denotes Part I) for the E polarization, we see that the backscattering characteristics for the E and the H polarization are different from each other in all numerical examples. In particular, the monostatic RCS for the H polarization oscillates rapidly in comparison to the E-polarized case. This difference is due to the fact that the effect of edge diffraction depends explicitly on the incident polarization. Next we shall consider the region $0° \leq \theta_0 \leq 90°$ where the cavity aperture is visible from the incident direction. In this region, the interior irradiation is dominant compared to the edge-diffracted fields. Comparing the RCS characteristics over $0° \leq \theta_0 \leq 90°$ between the E and the H polarization, we see that if the cavity dimensions are small as in Figs. 2a, 3a, 4a, I.4a, I.5a, and I.6a, there is a difference depending on the incident polarization. It is interesting to note from the figures that the RCS reduction near $\theta_0 = 0°$ for loaded cavities with $2b = \lambda$ is more significant in the H-polarized case. On the other hand, the results for both polarizations over $0° \leq \theta_0 \leq 90°$ show similar features with an increase of the cavity opening, as may be seen from Figs. 2c, 3c, 4c, I.4c, I.5c, and I.6c.

From Figs. 5–7, it is seen that in all numerical examples, the bistatic RCS shows the largest and the second largest values along the incident and reflected shadow boundaries at $\theta = -120°$ and $\theta = 120°$, respectively, as expected. Comparing the RCS curves for empty cavities with those for loaded cavities, the effect of material loading inside the cavity is clearly seen over $|\theta| < 90°$, as in the E polarization, and the RCS is reduced for loaded cavities. This is because, the cavity aperture is then visible from the observation point and the interior features of the cavity affect explicitly the far field bistatic scattering. On comparing the results for loaded cavities of $2b = 5\lambda$ and 10λ in Figs. 5–7 with those in Figs. I.7–I.9 generated for the E-polarized case, we see that the RCS reduction due to material loading for negative θ is more significant in the H polarization. As regards the characteristics over the range $110° < |\theta| < 180°$, it has been pointed out in Part I that the bistatic RCS for both empty and loaded cavities shows close features in the E polarization. For the H-polarized case, however, there appear some differences over that range depending on the material inside the cavity. Therefore, it is inferred that for the H polarization, a difference on the interior features of the cavity affects the far field bistatic scattering even in the region where the cavity aperture is invisible from the observer.

We shall now make some comparisons with the results due to a high-frequency technique. In Figs. 8 and 9, the present Wiener-Hopf solution is compared with the results generated by Burkholder [11] using the hybrid asymptotic-modal approach together with the geometrical theory of diffraction (GTD), where solid lines and dots denote the Wiener-Hopf results and Burkholder's results, respectively. As mentioned in Part I, Burkholder applied the hybrid asymptotic-modal approach for the interior scattering and the first order GTD for the exterior scattering due to the leading edges at $z = L$ and the right-angled back corners at $z = -L$. In addition, he uses the half-plane diffraction coefficient approximately to find the scattering effect from the leading edges of loaded cavities. It is noted from Fig. 8 for empty cavities that Burkholder's results agree very well with the present Wiener-Hopf solution over the whole range shown in the figures. Comparing the results in Fig. 8 with those in Fig. I.10, we see that the agreement is better in the H-polarized case. It is also found from Fig. 9 that, although Burkholder accounts for the diffraction by the leading edges approximately for loaded cavities, his results are still in reasonably good agreement with our rigorous Wiener-Hopf solution.

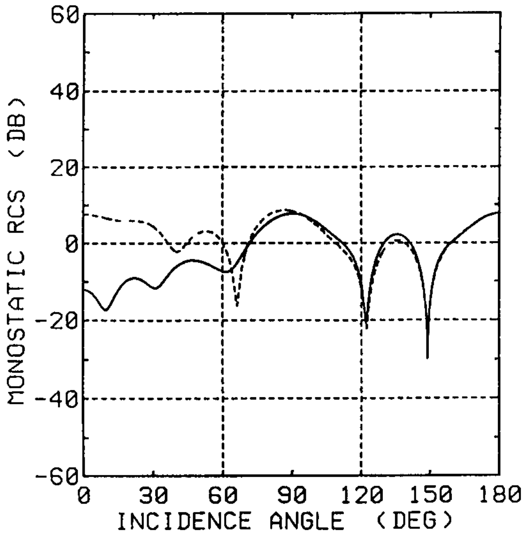

Figure 2a. Monostatic RCS σ/λ [dB] for $L/b = 1.0$, $2b = \lambda$. Solid lines and dashed lines denote the results for a material-loaded cavity with $\varepsilon_r = 2.5 + i1.25, \mu_r = 1.6 + i0.8$ and an empty cavity, respectively.

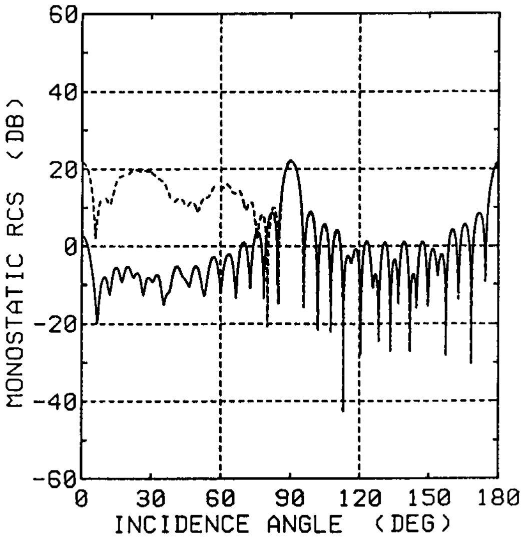

Figure 2b. Monostatic RCS σ/λ [dB] for $L/b = 1.0$, $2b = 5\lambda$. Other particulars are the same as in Fig. 2a.

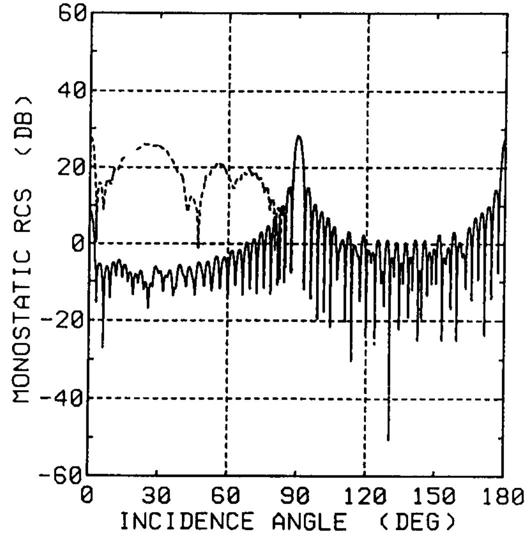

Figure 2c. Monostatic RCS σ/λ [dB] for $L/b = 1.0$, $2b = 10\lambda$. Other particulars are the same as in Fig. 2a.

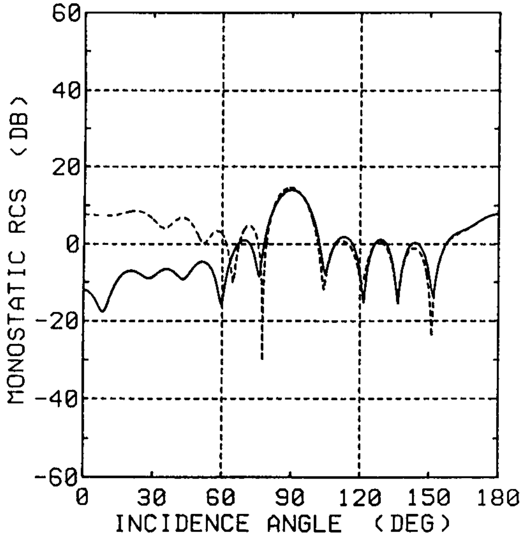

Figure 3a. Monostatic RCS σ/λ [dB] for $L/b = 2.0$, $2b = \lambda$. Other particulars are the same as in Fig. 2a.

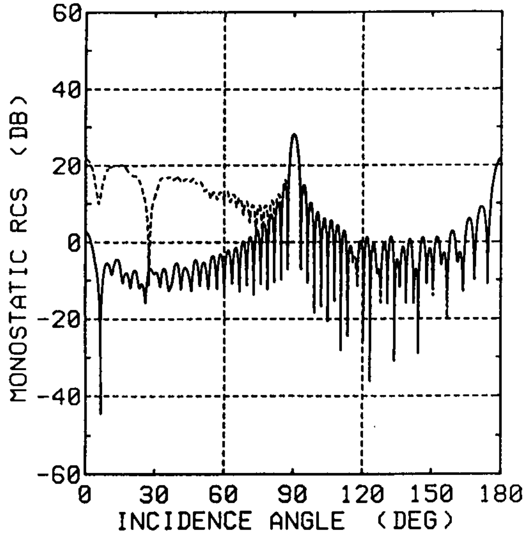

Figure 3b. Monostatic RCS σ/λ [dB] for $L/b = 2.0, 2b = 5\lambda$. Other particulars are the same as in Fig. 2a.

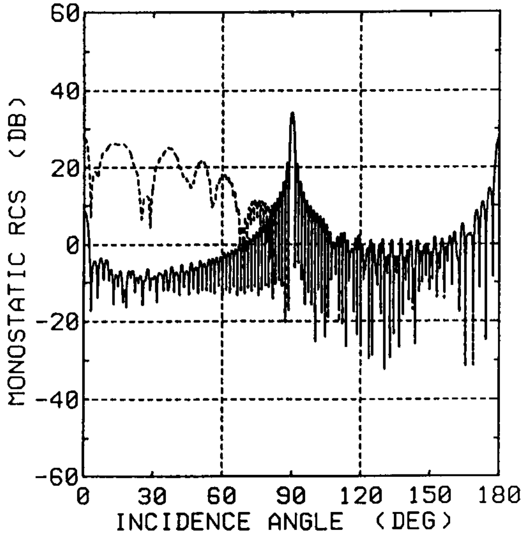

Figure 3c. Monostatic RCS σ/λ [dB] for $L/b = 2.0$, $2b = 10\lambda$. Other particulars are the same as in Fig. 2a.

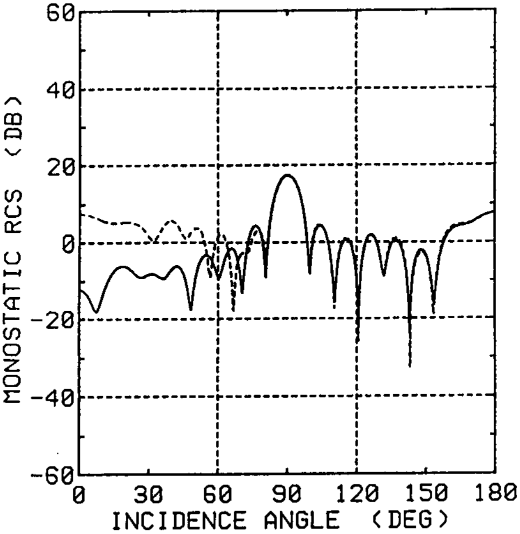

Figure 4a. Monostatic RCS σ/λ [dB] for $L/b = 3.0$, $2b = \lambda$. Other particulars are the same as in Fig. 2a.

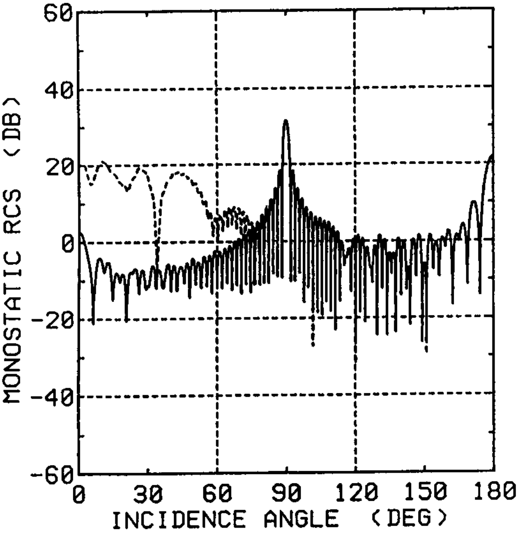

Figure 4b. Monostatic RCS σ/λ [dB] for $L/b = 3.0$, $2b = 5\lambda$. Other particulars are the same as in Fig. 2a.

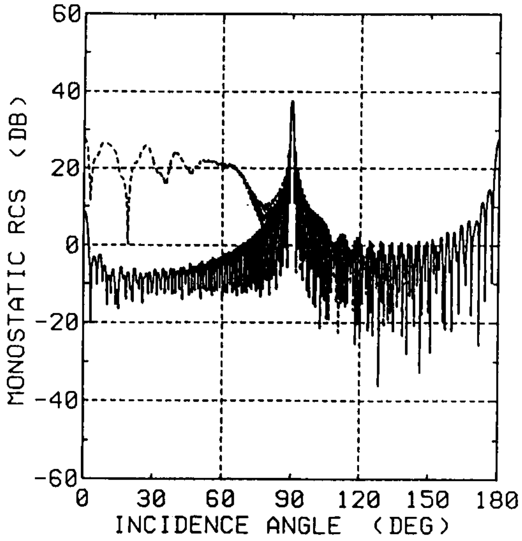

Figure 4c. Monostatic RCS σ/λ [dB] for $L/b = 3.0$, $2b = 10\lambda$. Other particulars are the same as in Fig. 2a.

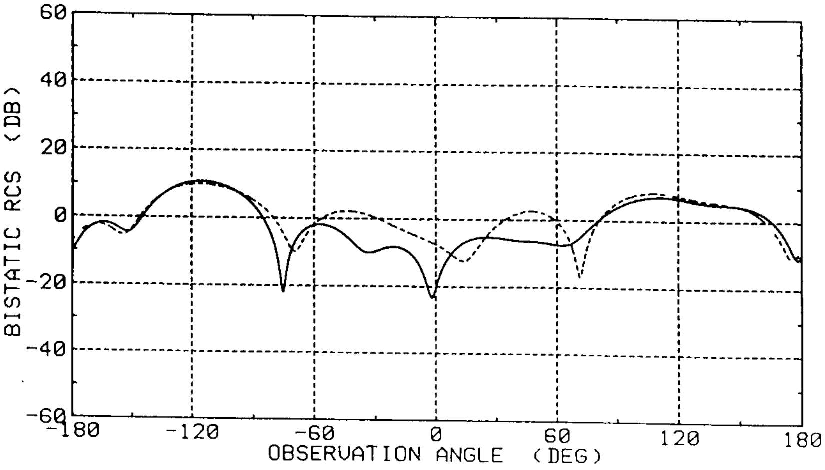

Figure 5a. Bistatic RCS σ/λ [dB] for $L/b = 1.0$, $2b = \lambda$, $\theta_0 = 60°$. Solid lines and dashed lines denote the results for a material-loaded cavity with $\varepsilon_r = 2.5 + i1.25, \mu_r = 1.6 + i0.8$ and an empty cavity, respectively.

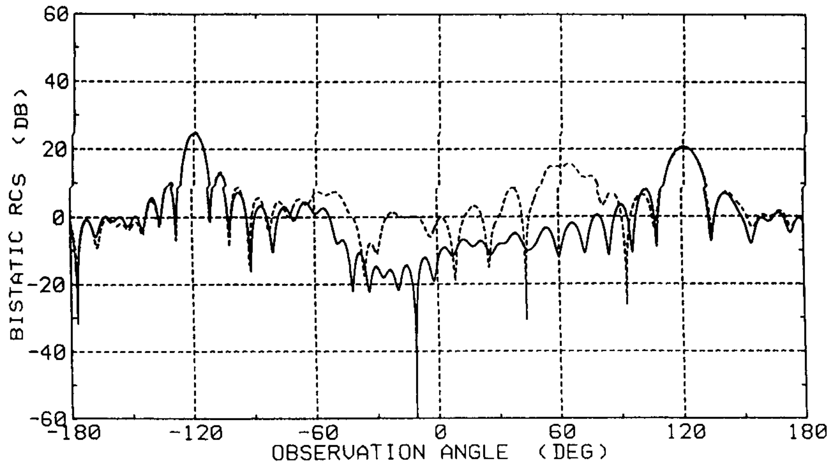

Figure 5b. Bistatic RCS σ/λ [dB] for $L/b = 1.0$, $2b = 5\lambda$, $\theta_0 = 60°$. Other particulars are the same as in Fig. 5a.

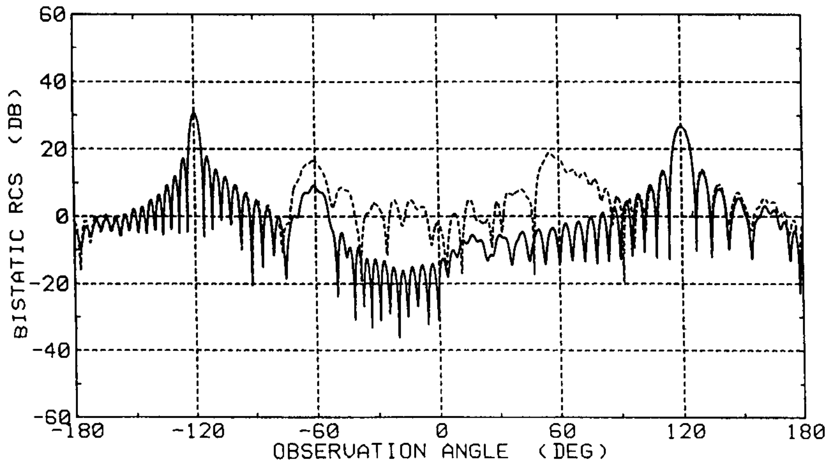

Figure 5c, Bistatic RCS σ/λ [dB] for $L/b = 1.0$, $2b = 10\lambda$, $\theta_0 = 60°$. Other particulars are the same as in Fig. 5a.

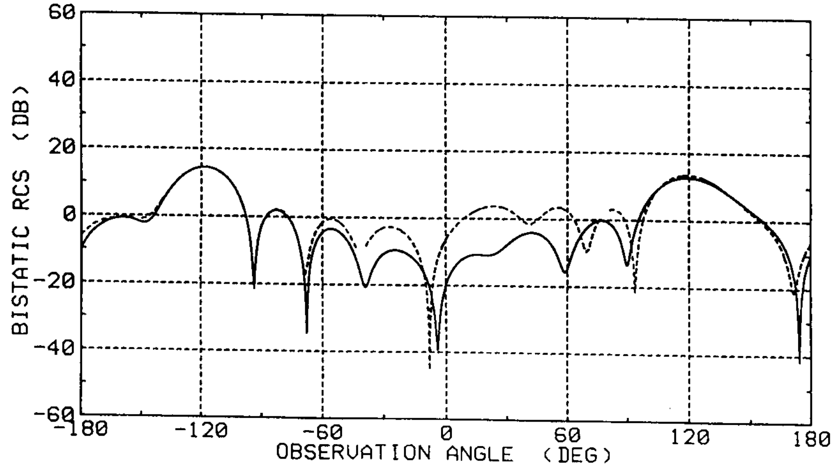

Figure 6a. Bistatic RCS σ/λ [dB] for $L/b = 2.0$, $2b = \lambda$, $\theta_0 = 60°$. Other particulars are the same as in Fig. 5a.

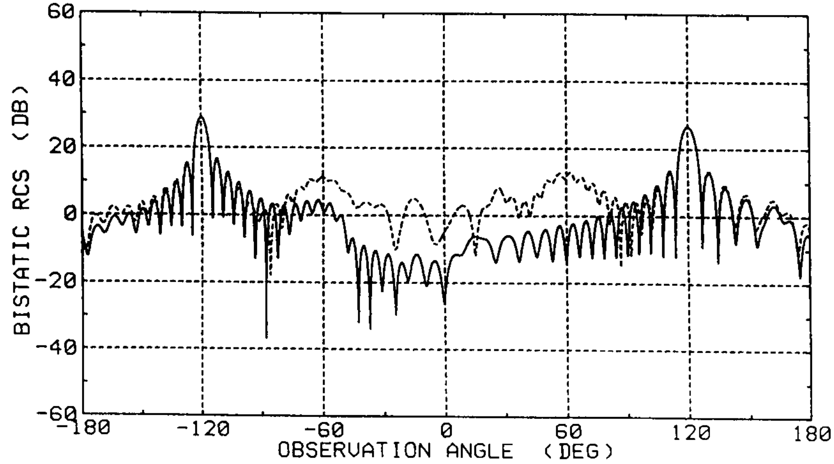

Figure 6b. Bistatic RCS σ/λ [dB] for $L/b = 2.0$, $2b = 5\lambda$, $\theta_0 = 60°$. Other particulars are the same as in Fig. 5a.

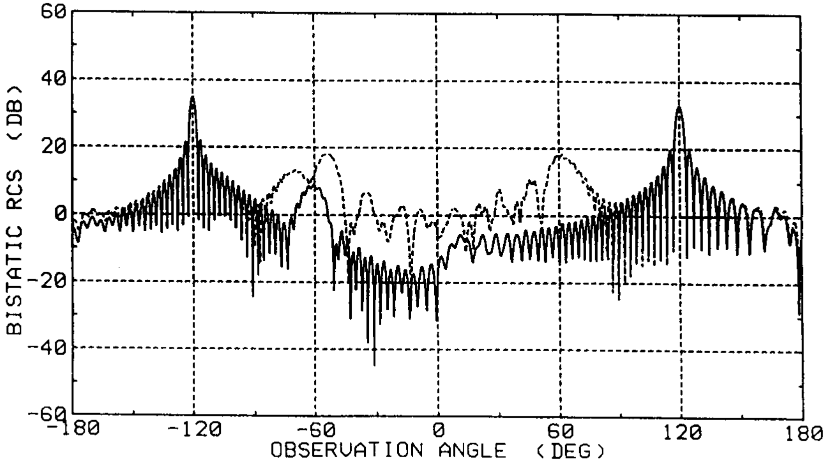

Figure 6c. Bistatic RCS σ/λ [dB] for $L/b = 2.0$, $2b = 10\lambda$, $\theta_0 = 60°$. Other particulars are the same as in Fig. 5a.

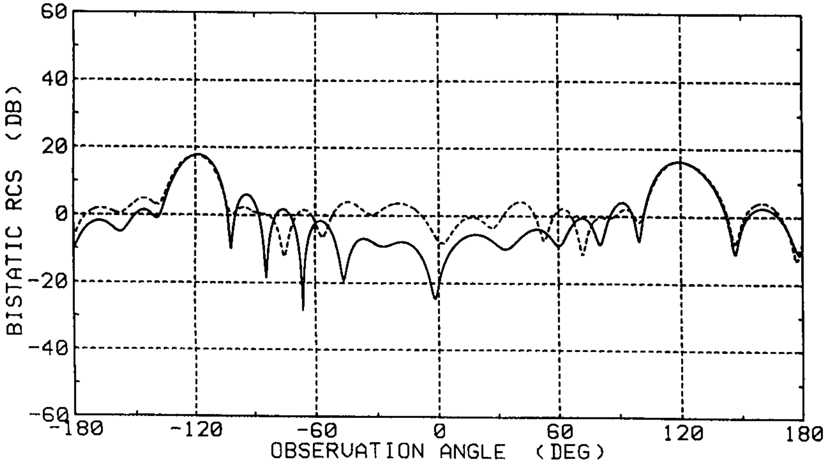

Figure 7a. Bistatic RCS σ/λ [dB] for $L/b = 3.0$, $2b = \lambda$, $\theta_0 = 60°$. Other particulars are the same as in Fig. 5a.

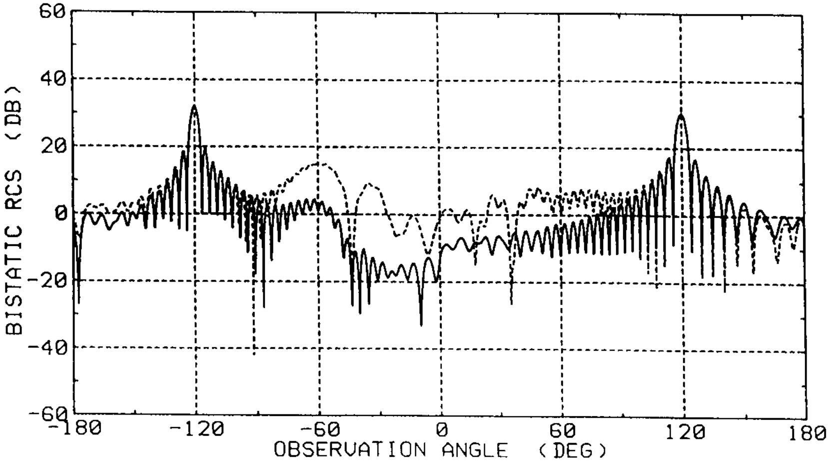

Figure 7b. **Bistatic RCS** σ/λ **[dB] for** $L/b = 3.0$, $2b = 5\lambda$, $\theta_0 = 60°$. **Other particulars are the same as in Fig. 5a.**

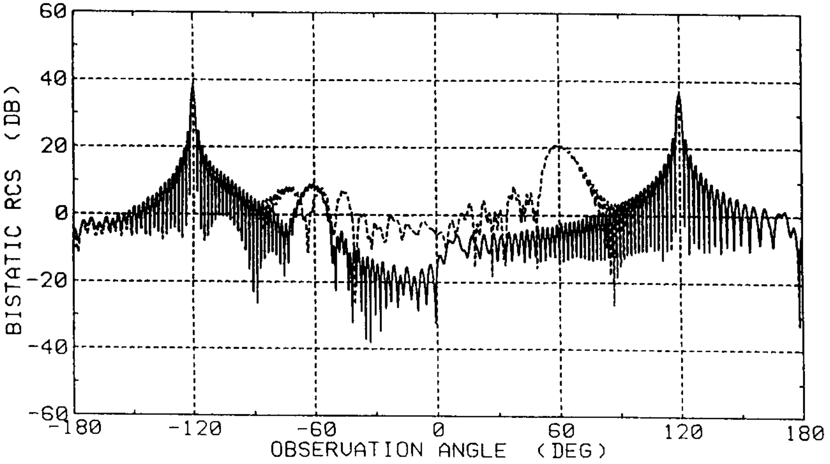

Figure 7c. **Bistatic RCS** σ/λ **[dB] for** $L/b = 3.0$, $2b = 10\lambda$, $\theta_0 = 60°$. **Other particulars are the same as in Fig. 5a.**

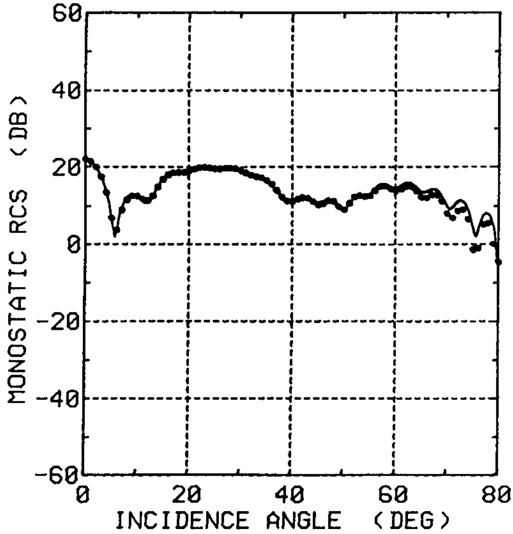

Figure 8a. Monostatic RCS σ/λ [dB] of an empty cavity with $L/b = 1.0$, $2b = 5\lambda$ and its comparison with Burkholder [11]. Solid lines and dots denote the results of this paper and Burkholder's results, respectively.

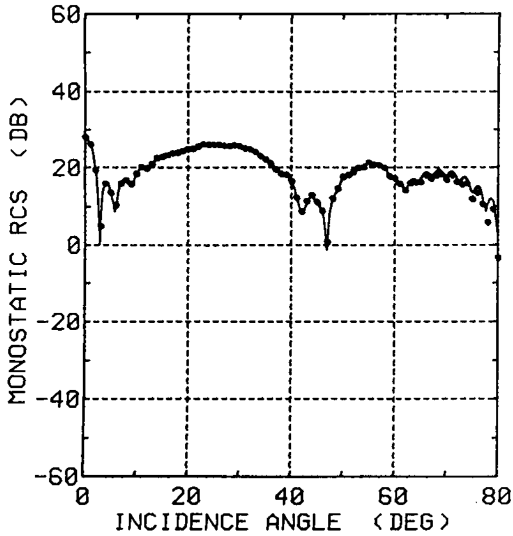

Figure 8b. Monostatic RCS σ/λ [dB] of an empty cavity with $L/b = 1.0$, $2b = 10\lambda$ and its comparison with Burkholder [11]. Other particulars are the same as in Fig. 8a.

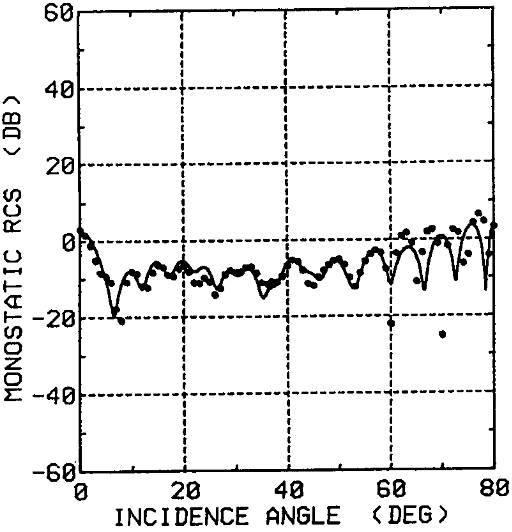

Figure 9a. Monostatic RCS σ/λ [dB] of a material-loaded cavity with $L/b = 1.0$, $2b = 5\lambda, \varepsilon_r = 2.5 + i1.25$, $\mu_r = 1.6 + i0.8$ and its comparison with Burkholder [11]. Other particulars are the same as in Fig. 8a.

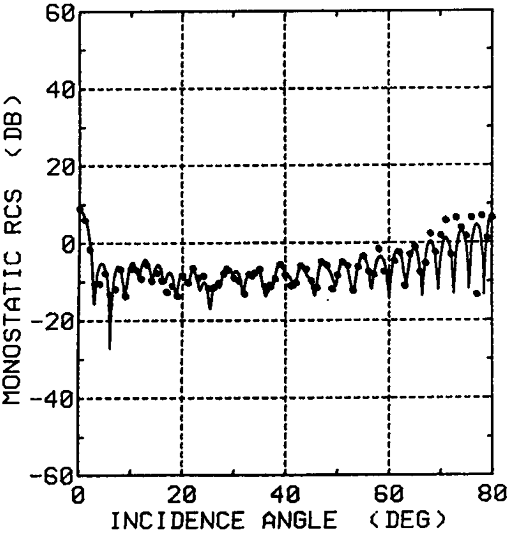

Figure 9b. Monostatic RCS σ/λ [dB] of a material-loaded cavity with $L/b = 1.0, 2b = 10\lambda$, $\varepsilon_r = 2.5 + i1.25$, $\mu_r = 1.6 + i0.8$ and its comparison with Burkholder [11]. Other particulars are the same as in Fig. 8a.

7. Conclusions

In this second part of a two-part paper, we have analyzed rigorously the plane wave diffraction by a parallel-plate waveguide cavity with dielectric/ferrite loading for the H polarization using the Wiener-Hopf technique. Unlike most of the other existing methods, the Wiener-Hopf technique takes into account the edge condition rigorously and incorporates all the possible effects of the scattering from the interior and the exterior of the cavity. Hence, our final approximate solution presented in this paper is uniformly valid in incidence and observation angles as well as in cavity dimensions unless the cavity depth is too small in comparison to the wavelength. Based on these results, we have carried out numerical computations and given representative numerical examples on the monostatic RCS and the bistatic RCS to discuss the scattering characteristics of the cavity in detail. Some remarks on the polarization difference have also been given by comparing the results with those obtained in Part I for the E-polarized case. The results have also been compared with a high-frequency technique.

Acknowledgments

The authors would like to thank Professor Kazuo Horiuchi of Waseda University for many helpful discussions. They are also indebted to Dr. Robert J. Burkholder of The Ohio State University for providing the RCS data in Figs. 8 and 9. This work was supported in part by the 1992 Chuo University Special Research Grant.

References

[1] Kobayashi, K., and A. Sawai, "Plane wave diffraction by an open-ended parallel plate waveguide cavity," *J. Electromagnetic Waves Applic.*, Vol. 6, No. 4, 475–512, 1992.

[2] Kobayashi, K., "Some diffraction problems involving modified Wiener-Hopf geometries," in *Analytical and Numerical Methods in Electromagnetic Wave Theory,* Chap. 4, M. Hashimoto, M., Idemen, and O. A. Tretyakov, Eds., Science House, Tokyo, 1993.

[3] Koshikawa, S., and K. Kobayashi, "Diffraction by a parallel-plate waveguide cavity with a thick planar termination," *IEICE Trans. Electron.*, Vol. E76-C, No. 1, 142–158, Jan. 1993.

[4] Kobayashi, K., S. Koshikawa, and A. Sawai, "Diffraction by a parallel-plate waveguide cavity with dielectric/ferrite loading: Part I–The case of E polarization," J. A. Kong, Ed., *Progress in Electromagnetics Research,* PIER 8, 377–426, 1994.

[5] Noble, B., *Methods Based on the Wiener-Hopf Technique for the Solution of Partial Differential Equations,* Pergamon Press, London, 1958. See also, second edition, Chelsea Publishing, New York, 1988.

[6] Mittra, R., and S.-W. Lee, *Analytical Techniques in the Theory of Guided Waves,* Macmillan, New York, 1971.

[7] Kobayashi, K., "The Wiener-Hopf technique with applications to scattering and diffraction problems," in *A Course of Applied Mathematics,* Chap. 9 (in Japanese), K. Horiuchi, Ed., Corona Publishing, Tokyo, 1989.

[8] Kobayashi, K., "On generalized Gamma functions occurring in diffraction theory," *J. Phys. Soc. Japan,* Vol. 60, No. 5, 1501–1512, May 1991.

[9] Meixner, J., "The behavior of electromagnetic fields at edges," *Res. Rep., Div. Electromagnetic Res.,* Inst. Math. Sci., New York Univ., No. EM-72, 1954. See also, J. Meixner, *IEEE Trans. Antennas Propagat.,* Vol. AP-20, No. 4, 442–446, July 1972.

[10] Lee, S.-W., and H. Ling, "Data book for cavity RCS: Version 1," *Tech. Rep.,* No. SWL89-1, Univ. Illinois, Urbana, Jan. 1989.

[11] Burkholder, R. J., private communication, Nov. 1992.